DRAFT VERSION JANUARY 13, 2025
Typeset using LaTeX **preprint2** style in AASTeX631

Discovery of a likely Type II SN at z=3.6 with *JWST*

D. A. COULTER,[1] J. D. R. PIEREL,[1,*] C. DECOURSEY,[2] T. J. MORIYA,[3,4,5] M. R. SIEBERT,[1] B. A. JOSHI,[6] M. ENGESSER,[1] A. REST,[1,6] E. EGAMI,[2] M. SHAHBANDEH,[1] W. CHEN,[7] O. D. FOX,[1] L. G. STROLGER,[1] Y. ZENATI,[6,1,†] A. J. BUNKER,[8] P. A. CARGILE,[9] M. CURTI,[10] D. J. EISENSTEIN,[9] S. GEZARI,[1,6] S. GOMEZ,[9] M. GUOLO,[6] K. HAINLINE,[2] J. JENCSON,[11] B. D. JOHNSON,[9] M. KARMEN,[6] R. MAIOLINO,[12,13,14] R. M. QUIMBY,[15,16] P. RINALDI,[2] B. ROBERTSON,[17] S. TACCHELLA,[12,13] F. SUN,[9] Q. WANG,[18] AND T. WEVERS[1]

[1]*Space Telescope Science Institute, Baltimore, MD 21218, USA*
[2]*Steward Observatory, University of Arizona, 933 N. Cherry Avenue, Tucson, AZ 85721, USA*
[3]*National Astronomical Observatory of Japan, National Institutes of Natural Sciences, 2-21-1 Osawa, Mitaka, Tokyo 181-8588, Japan*
[4]*Graduate Institute for Advanced Studies, SOKENDAI, 2-21-1 Osawa, Mitaka, Tokyo 181-8588, Japan*
[5]*School of Physics and Astronomy, Monash University, Clayton, VIC 3800, Australia*
[6]*Physics and Astronomy Department, Johns Hopkins University, Baltimore, MD 21218, USA*
[7]*Department of Physics, Oklahoma State University, 145 Physical Sciences Bldg, Stillwater, OK 74078, USA*
[8]*Department of Physics, University of Oxford, Denys Wilkinson Building, Keble Road, Oxford OX1 3RH, UK*
[9]*Center for Astrophysics | Harvard & Smithsonian, 60 Garden St., Cambridge MA 02138 USA*
[10]*European Southern Observatory, Karl-Schwarzschild-Strasse 2, 85748 Garching, Germany*
[11]*IPAC, Mail Code 100-22, Caltech, 1200 E. California Boulevard, Pasadena, CA 91125, USA*
[12]*Kavli Institute for Cosmology, University of Cambridge, Madingley Road, Cambridge CB3 0HA, UK*
[13]*Cavendish Laboratory, University of Cambridge, 19 JJ Thomson Avenue, Cambridge, CB3 0HE, UK*
[14]*Department of Physics and Astronomy, University College London, Gower Street, London WC1E 6BT, UK*
[15]*Department of Astronomy/Mount Laguna Observatory, San Diego State University, 5500 Campanile Drive, San Diego, CA 92812-1221, USA*
[16]*Kavli Institute for the Physics and Mathematics of the Universe (WPI), The University of Tokyo Institutes for Advanced Study, The University of Tokyo, Kashiwa, Chiba 277-8583, Japan*
[17]*Department of Astronomy and Astrophysics, University of California, Santa Cruz, 1156 High Street, Santa Cruz CA 96054, USA*
[18]*Department of Physics and Kavli Institute for Astrophysics and Space Research, Massachusetts Institute of Technology, 77 Massachusetts Avenue, Cambridge, MA 02139, USA*

ABSTRACT

Transient astronomy in the early, high-redshift ($z > 3$) Universe is an unexplored regime that offers the possibility of probing the first stars and the Epoch of Reionization. During Cycles 1 and 2 of the *James Webb Space Telescope* (*JWST*), the *JWST* Advanced Deep Extragalactic Survey (JADES) program enabled one of the first searches for transients in deep images ($\sim$30 AB mag) over a relatively wide area (25 arcmin^2). One transient, AT 2023adsv, was discovered with an F200W magnitude of 28.04 AB mag, and subsequent *JWST* observations revealed that the transient is a likely supernova (SN) in a host with $z_{\rm spec} = 3.613 \pm 0.001$,

Corresponding author: D. A. Coulter
dcoulter@stsci.edu

a host mass of $\log(M_*/M_\odot) = 8.41^{+0.12}_{-0.12}$, and an inferred metallicity at the position of the SN of $Z_* = 0.3 \pm 0.1\ Z_\odot$. At this redshift, the first detections in F115W and F150W show that AT 2023adsv had bright rest-frame ultraviolet flux at the time of discovery. The multi-band light curve of AT 2023adsv is best matched by a template of an SN IIP, with a peak absolute magnitude of -18.3 AB mag in the rest-frame B-band. We model AT 2023adsv's light curve and find a good match to a $20M_\odot$ red supergiant progenitor star with an explosion energy of 2.0×10^{51} ergs, likely higher than normally observed in the local Universe, but consistent with SNe IIP drawn from local, lower metallicity environments. AT 2023adsv is the most distant photometrically classified SN IIP yet discovered with a spectroscopic redshift measurement, and may represent a global shift in SNe IIP properties as a function of redshift. This discovery, and the ones sure to follow, demonstrate the continued need for facilities like *JWST* to build a statistical sample of core-collapse SNe to understand the evolution of their properties, and to constrain the poorly understood relationship between progenitor metallicity and massive star evolution.

Keywords: supernovae: individual (AT 2023adsv); SN II - infrared: supernovae - stars: massive - galaxies: abundances

1. INTRODUCTION

Core-collapse supernovae (CCSNe) are the explosive deaths of massive stars with initial masses $> 8\ M_\odot$ and are remarkably diverse in their properties (Oppenheimer & Snyder 1939; Kobulnicky & Skillman 1997; Vanbeveren et al. 1998; Heger et al. 2003; Smartt 2009; Dessart & Hillier 2020; Burrows & Vartanyan 2021). This diversity is driven by the broad range of their progenitor masses, which sensitively affect their evolution, setting the initial conditions for both their stellar structure and circumstellar environments prior to collapse and resulting in a similarly broad range of explosion energies, ejecta compositions and observed luminosities (Smith 2014; Gal-Yam et al. 2014; Wu & Fuller 2021). These explosions connect to astrophysical phenomena across many scales — due to their high mass, the progenitors of CC SNe have short lifetimes and therefore trace the instantaneous star formation rate (SFR) of their locales; their rates constrain the high-mass end of the Initial Mass Function (IMF); their explosions deposit energy and momentum into the interstellar medium (ISM) providing a feedback mechanism to moderate star formation; they enrich the ISM with metals and are factories for cosmic dust; and they produce ionizing photons that contribute to the reionization of the Universe.

CC SNe, and in particular SNe II, are in principle luminous enough to be observed at cosmological distances, making them intriguing probes of the early Universe. However, their peak emission in optical bands is shifted into the infrared (IR) at high-redshift. In the last two decades, work based on the *Hubble Space Telescope* (*HST*) has pushed the study of CCSNe rates and properties to further distances (Botticella et al. 2008; Bazin et al. 2009; Graur et al. 2011; Melinder et al. 2012; Dahlen et al. 2012), culminating with observations from the Cosmic Assembly Near-infrared Deep Extragalactic Legacy Survey (CANDELS; Grogin et al. 2011; Koekemoer et al. 2011) and Cluster Lensing And Supernova survey with Hubble (CLASH; Postman et al. 2012), which constrained the CCSN rate out to $z \approx 2.5$ (Strolger et al. 2015).

CC SNe discovered at even greater distances ($z > 2.5$) will peak in at wavelengths of 2 μm

* NASA Einstein Fellow
† ISEF International Fellowship

and beyond, placing more distant samples out of reach for *HST* but not of the *James Webb Space Telescope* (*JWST*). Indeed, *JWST* is already removing this barrier to discovering distant and observer-frame IR bright CC SNe due to its combination of wavelength coverage and sensitivity, opening a new frontier in transient astronomy with the discovery of several high-z SNe since its launch (Chen et al. 2022; Engesser et al. 2022a,b; DeCoursey et al. 2023a,b,c, 2024; Pierel et al. 2024a,b,c,d; Siebert et al. 2024). Such discoveries are vital laboratories to test topics such as whether the CC SN rate follows the cosmic SFR density or if the high-mass end of the IMF flattens with redshift in low metallicity stellar populations (Larson 1998; Ziegler et al. 2022).

While metallicity could very plausibly impact the rate of CC SNe, it also impacts their massive stellar progenitors and, therefore, their explosive properties. In particular, the metallicity of the progenitors to SNe II affects not only their mass loss (Vink et al. 2001; Mokiem et al. 2007), but their internal structure and convective efficiency (Heger et al. 2003; Dessart et al. 2013), leading to a range of pre-explosion envelope masses, stellar radii, and the presence of circumstellar material (CSM). These, in turn, yield a diversity of observed SN II properties, such as their resulting colors, peak luminosities, and for SNe IIP, their plateau durations (Sanyal et al. 2017; Dessart et al. 2013). In general, lower metallicities should lead to lower mass loss rates for SN II progenitors, yielding more massive progenitors (barring interactions with binary companions; Lamers & Cassinelli 1999; Kudritzki & Puls 2000), and the reduction in stellar envelope opacity should result in stars with smaller stellar radii (Sanyal et al. 2017). These effects may combine to produce progenitors with substantially higher rotation rates (Woosley & Heger 2006; Maeder & Meynet 2012) and potentially connect lower metallicity environments at high-z with a diverse menagerie of exotic SN types including pair-instability SNe (PISNe; Kasen et al. 2011; Woosley 2017), superluminous supernovae (SLSNe; Quimby et al. 2011; Gal-Yam 2019), and the supernovae associated with long gamma-ray bursts (LGRB; Zeh et al. 2004; Fruchter et al. 2006; Modjaz et al. 2014). However, these assertions need to be tested through the discovery of many more CC SNe in the early Universe.

Fortunately, this is a task to which *JWST* is particularly well-suited. The *JWST* Advanced Deep Extragalactic Survey (JADES) program (Eisenstein et al. 2023) observed $\sim$ 25 arcmin^2 of the sky to depths of $m_{AB} \gtrapprox 30$ in 9 NIRCam filters in two separate epochs, the first between September 29 and October 5, 2022, and the second between September 28 and October 3, 2023. These repeated observations allowed for these images to be subtracted to discover new transients beyond the redshift limitations of *HST*, with a sensitivity for CCSNe to $z > 4$. Using this $\sim$ 1 year baseline dozens of new transient objects were discovered (DeCoursey et al. 2024, hereafter D24), and here we present a candidate for one of the most distant SN II discovered to date: AT 2023adsv, a very blue and likely sub-solar metallicity SN IIP-like transient located at R.A.=3h32m39.4574s decl.=$-$27d50m19.6660s (although see Cooke et al. (2012) and Gomez et al. (2024) for previous high-z SLSNe candidates). AT 2023adsv is embedded in its host, JADES-GS+53.16439-27.83877, with a spectroscopically confirmed redshift of $z_{\rm spec} = 3.613 \pm 0.001$.

In what follows, we describe the identification and analysis of AT 2023adsv, as well as a brief comparison to other SNe IIP in the local universe. This paper is structured as follows: in §2, we present a summary of the observations for this supernova, our reduction of the data, and obtaining AT 2023adsv's host redshift; in §3 we describe our classification of AT 2023adsv as a likely SN II and present the properties of its host and model AT 2023adsv's light curve, in §4 we discuss AT 2023adsv in the context of a sample of local SNe IIP, and in §5 we conclude with a dis-

cussion on the prospects for building an SNe IIP sample at high redshift and its use as a metallicity probe of the Universe, as well as the implications of the new frontier enabled by *JWST*. Throughout this paper, we assume a standard ΛCDM cosmology with $H_0 = 70$km s^{-1} Mpc^{-1}, $\Omega_m = 0.315$.

2. SUMMARY OF OBSERVATIONS

AT 2023adsv was discovered as a part of a transient search for the JADES program (Eisenstein et al. 2023), centered on the Great Observatories Origins Deep Survey's south field (GOODS-S; Giavalisco et al. 2004). A full description of JADES, including its survey design, data products, the selection process for discovering new transients, and the follow-up observations of those subsequent discoveries through its approved DDT program, are described and presented in detail in D24.

To summarize, the first JADES observations were acquired between September 29th, 2022 and October 5th, 2022, in the NIRCam filters F090W, F115W, F150W, F200W, F277W, F335M, F356W, F410M, and F444W to a 5σ depth of $m_{AB} \sim 30$. Nearly a year later, a second set of observations in the same filters and to the same depths were taken between September 29th, 2023 and October 3rd, 2023, resulting in an overlapping footprint of $\sim$ 25 arcmin^2 (both observations under PID 1180). During this second epoch, several observations failed, and subsets of the field were observed on November 15th, 2023, and January 1st, 2024. Upon the identification of many interesting transients in color, redshift, and luminosity space (see D24 for a complete accounting), a *JWST* Director's Discretionary Time (DDT) program was approved to follow up the most interesting transients in this field (Egami et al. 2023). These subsequent observations were obtained on November 28th, 2023 (NIRCam filters F115W, F150W, F200W, F277W, F356W, and F444W) and on January 1st, 2024 (NIRCam filters F150W, F200W, F277W, F356W, and F444W; PID 6541) with the latter epoch including NIRSpec multi-object spectroscopy (MOS) coverage using the micro-shutter assembly (MSA; Ferruit et al. 2022). NIRSpec covered the most promising $\sim$ 10 transients (as well as a variety of galaxy spectra) using the MSA with the Prism (R$\sim$ 100) grating, of which AT 2023adsv was one, as well as two others that are described in a pair of companion papers (Pierel et al. 2024c; Siebert et al. 2024). Below, we describe the data reduction and photometric measurements we derive for AT 2023adsv.

2.1. *Measuring Photometry*

AT 2023adsv is embedded in a relatively compact host and therefore obtaining accurate photometric measurements requires removing the underlying host light from the SN position. We achieve this through the process of "difference imaging," or subtracting a template image (preferably with no SN light in it) from a series of science images containing the SN flux we wish to measure. For every science epoch, we align each of the underlying *JWST* Level 2 (CAL) images to a catalog of JADES galaxies (that has in turn been aligned to *Gaia* sources), using the *JWST*/*HST* Alignment Tool (`JHAT`; Rest et al. 2023)[1]. CAL images are those that have been bias-subtracted, dark-subtracted, and flat-fielded but not yet corrected for geometric distortion. We drizzle these CAL files into Level 3 (I2D) files using the *JWST* pipeline (Bushouse et al. 2022). The extra JHAT step improves the relative alignment by an order of magnitude between the epochs (from $\sim$ 1 pixel to $\sim$ 0.1 pixel), allowing for subtractions with fewer artifacts between the template and science images. To perform the subtraction, we use the High Order Transform of PSF and Template Subtraction (`HOTPANTS`; Becker 2015)[2] code (with additional improvements implemented in `photpipe`; Rest et al. 2005), resulting in the difference images upon which we perform our photometry (see Figure 1; the right three columns are the difference images

[1] https://jhat.readthedocs.io
[2] https://github.com/acbecker/hotpants

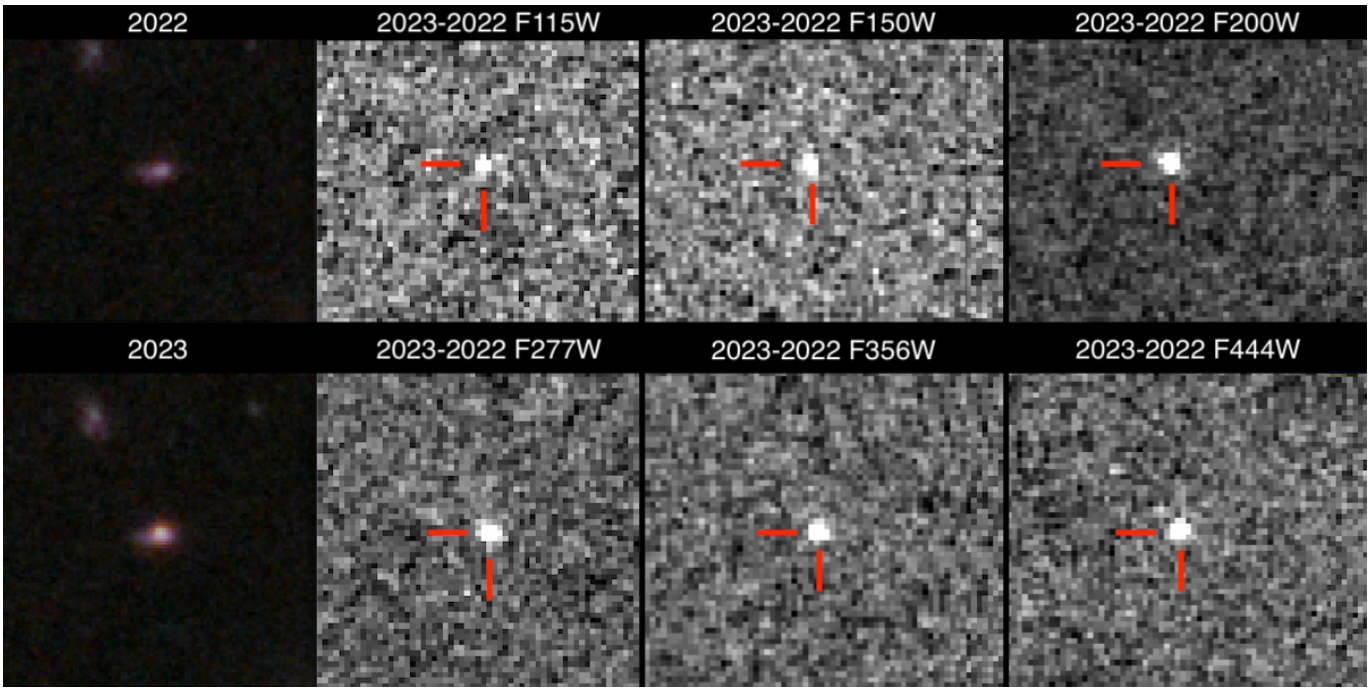

Figure 1. (Left column) Full color images using F115W+F150W (Blue) F200W+F277W (Green) and F356W+F444W (Red), with the 2022 JADES epoch on top and 2023 (including AT 2023adsv) on the bottom. (Column 2-4) Difference images were created from the two JADES epochs (2023 − 2022), with the AT 2023adsv position marked with a red indicator. All images are drizzled to $0.03''$/pix and have the same spatial extent.

[per filter] generated from subtracting the "template" [top, leftmost epoch] from the "science" image [bottom, leftmost image]).

We measure the photometry in the difference images with a process described in Pierel et al. (2024b,d), using the `space_phot`[3] Level 3 point-spread function (PSF) fitting routine centered on a 5×5 pixel cutout at AT 2023adsv's position. `space_phot` models the Level 3 PSF by drizzling the Level 2 PSF models from `webbpsf`[4], which account for the spatial and temporal dependence of the *JWST* PSF and corrects for the losses in flux incurred by imposing a finite aperture. The resulting fluxes, measured in units of MJy/sr, are converted to AB magnitudes using the native pixel scale of each image ($0.03''$/pix for short- and $0.06''$/pix for long-wavelength), and the final, measured photometry is given in Table 1.

2.2. *NIRSpec Reduction*

We obtained the Stage 2 spectroscopic data collected from the DDT program from the Mikulski Archive for Space Telescopes (MAST; see Table 2). With the context file `jwst_1185.pmap`, we used the *JWST* pipeline (Bushouse et al. 2022) to generate the two-dimensional (2D) spectrum and applied a correction for slit-losses based on the position of the SN within the MSA shutters (Figure 2, a and b). Next, we performed an optimal point source extraction using the algorithm from Horne (1986, implemented as a Jupyter notebook as part of the NIRSpec IFU Optimal Point Source Extraction guide[5]) to extract the superimposed spectra of the SN and its host. For an SN II, we expect Hα to be the brightest feature during the photospheric phase, and in our last epoch (when the spectrum was obtained, see Table 1) AT 2023adsv's flux in

[3] space-phot.readthedocs.io
[4] https://webbpsf.readthedocs.io
[5] https://spacetelescope.github.io/jdat_notebooks/notebooks/ifu_optimal/ifu_optimal.html

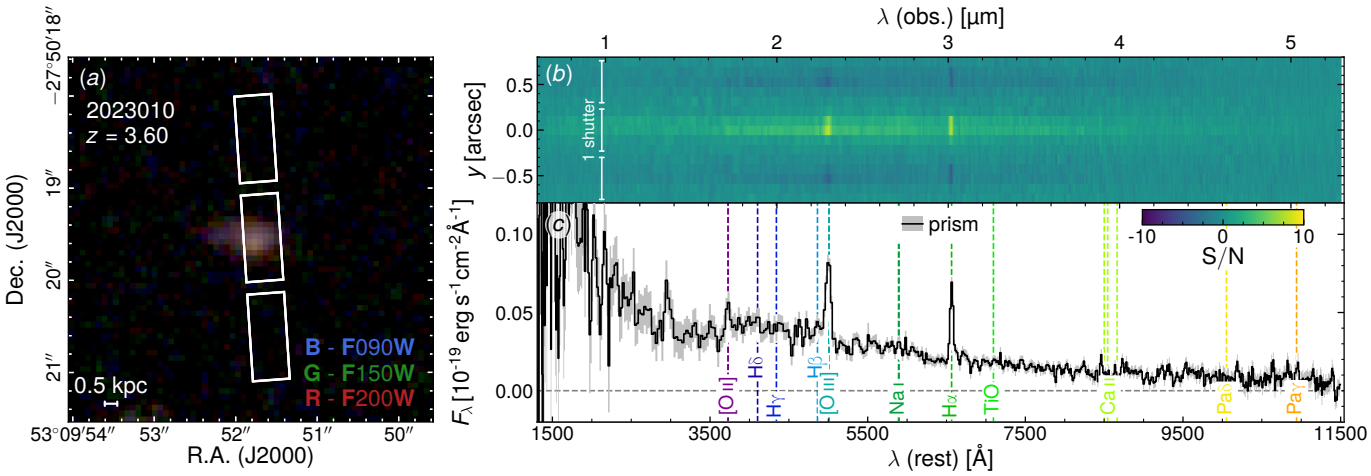

Figure 2. *a:* The MSA slitlet position over AT 2023adsv. *b:* The 2D NIRSpec Prism spectrum of AT 2023adsv and JADES-GS+53.16439-27.83877. *c:* The 1D-extracted NIRSpec spectrum for AT 2023adsv transformed into the rest-frame, with host emission lines color-coded and labeled. A spectroscopic redshift of $z = 3.613 \pm 0.001$ was measured based on the host's [O III] and Hα lines. No SN features are readily apparent in the resulting 1D spectrum.

Table 1. Observations for AT 2023adsv discussed in Section 2.

PID	MJD	Instrument	Filter/Grating	m_{AB}
1180	60216	NIRCam	F115W	30.04±0.12
1180	60216	NIRCam	F150W	28.83±0.06
1180	60217	NIRCam	F200W	28.07±0.04
1180	60216	NIRCam	F277W	27.94±0.04
1180	60217	NIRCam	F356W	27.99±0.05
1180	60216	NIRCam	F444W	28.14±0.06
1180	60276	NIRCam	F115W	>29.8
1180	60276	NIRCam	F150W	>29.5
1180	60276	NIRCam	F200W	28.49±0.13
1180	60276	NIRCam	F277W	28.17±0.12
1180	60276	NIRCam	F356W	28.03±0.11
1180	60276	NIRCam	F444W	28.25±0.21
6541	60310	NIRCam	F150W	>30.1
6541	60310	NIRCam	F200W	29.05±0.15
6541	60310	NIRCam	F277W	28.51±0.16
6541	60310	NIRCam	F356W	28.13±0.14
6541	60310	NIRCam	F444W	28.64±0.30
6541	60310	NIRSpec	Prism	–

NOTE—Columns are: *JWST* Program ID, Modified Julian date, *JWST* instrument, NIRCam filter, and photometry plus final uncertainty for AT 2023adsv. Upper limits are 5σ.

Table 2. AT 2023adsv NIRSpec Observation Details

Instrument	NIRSpec
Mode	MOS
Wavelength Range	$0.6 - 5.3\mu$m
Slit	3 Shutter ($0.46'' \times 0.2''$ each)
Grating/Filter	Prism/CLEAR
$R = \lambda/\Delta\lambda$	$\sim 30 - 300$
Readout Pattern	NRSIRS2
Groups per Integration	19
Integrations per Exposure	2
Exposures/Nods	3
Total Exposure Time	22,175s

F277W (near 3 μm) is $\sim$ 14 nJy while the flux in the spectrum is $\sim$ 50 nJy at the same wavelength. With nearly $3/4$ of the flux contaminated with host light, even if a decomposition were possible, the SN spectrum is likely to have a signal-to-noise of ~ 3 per pixel according to the *JWST* exposure time calculator[6]. For these reasons, we use the Prism spectrum primarily to measure AT 2023adsv's redshift (Figure 2, c), and the oxygen line ratios to estimate the host's metallicity (see Section 3.2).

[6] https://jwst-docs.stsci.edu/jwst-exposure-time-calculator-overview

2.3. *Host Galaxy Redshift*

AT 2023adsv was discovered in the host galaxy JADES-GS+53.16439-27.83877, and the first step in analyzing AT 2023adsv is to determine its host redshift by identifying prominent emission lines seen in Figure 2. These lines are best-matched by [O III] and Hα, which have rest-frame wavelengths of ~ 5008.24 Å and ~ 6564.61 Å in vacuum, respectively, and provide a robust spectroscopic redshift of $z_{\rm spec} = 3.613 \pm 0.001$. We use this value for all analyses going forward, and present a detailed analysis of these host properties in Section 3.2.

3. ANALYSIS

3.1. *SN Light Curve Matching*

We fit the measured photometry from Table 1 with the SALT3-NIR SN Ia light curve model (Pierel et al. 2022) and all existing CC SN light curve evolution models with rest-frame UV to near-IR (to observer-frame $\sim$ 4 μm) wavelength coverage (Pierel et al. 2018, and references therein). These models are empirical spectral templates created from extremely well-observed, low-z CC SNe and represent a wide range of diversity in each sub-type. In general, these spectral energy distributions (SEDs) are used to fit against our measured photometry, however, none of the templates extend to the rest-frame wavelengths covered by the F115W filter (~ 2500 Å), so it is excluded in the fitting (but see Section 3.3). We include Galactic dust based on the maps of Schlafly & Finkbeiner (2011) and the reddening law from Fitzpatrick (1999), which corresponds to $E(B-V) = 0.01$ mag with $R_V = 3.1$. We also allow for host galaxy dust (up to $E(B-V) = 1.5$ mag with $1 < R_V < 5$) of rest-frame, host-galaxy dust in the CC SN light curve fits and a SALT3-NIR color parameter range of $-1 < c < 1$.

Figure 3 shows the best fit models for each SN sub-type in all filters. The resulting χ^2 per degree of freedom (ν, or reduced-χ^2) for each model is shown in Table 3. The SN Ia and SN Ib/c subtypes are heavily disfavored (best fit $\chi^2/\nu = 16.63$ and 6.76, respectively) compared to SN II ($\chi^2/\nu = 1.10$). We take the results of this light curve fitting process as conclusive and give AT 2023adsv a classification of Type II as a result. The best fit SED to our photometry is that of SN 2006kv, a normal SN IIP discovered at $z = 0.0620$ (D'Andrea et al. 2010). We note, however, that the UV coverage of SN 2006kv's spectral template did not extend to cover AT 2023adsv's F115W detection (at $z = 3.61$, F115W ~ 2500 Å; see Figure 3), and therefore is omitted from the fitting. This blue emission could plausibly be due to a more exotic explosion with similarities to a SN II, a possibility that we explore in Section 3.3. While the fit to SN 2006kv is quite good (see Table 3), AT 2023adsv's luminosity required a modeled peak B-band absolute magnitude of -18.3 ± 0.1 mag, ~ 0.5 mag brighter relative to the real SN 2006kv; while this is still within the range of normal SN IIP absolute magnitudes observed in the local Universe ($\sim 3\sigma$ above the distribution mean (Richardson et al. 2014)), it is also in agreement with the suggestion from Scott et al. (2019) that low metallicity SN II could be up to ~ 0.5 mag brighter than SN II at high metallicity.

Table 3. Comparison of the best-fit model χ^2 statistic for each SN sub-type.

SN Type	Mode/Template	χ^2/ν
Ia	SALT3-NIR	16.63
Ib/c	SDSS004012	6.76
II	SN 2006kv	1.10

NOTE—Columns are: SN type, spectral model/template used, and the light curve fitting χ^2 per degree of freedom (DOF; ν) *without* model uncertainties, as they do not exist for CC SN models.

3.2. *Host Galaxy Properties*

At a redshift of $z = 3.61$, the host of AT 2023adsv opens a window into the environment of a SN when the Universe was < 2 Gyr old.

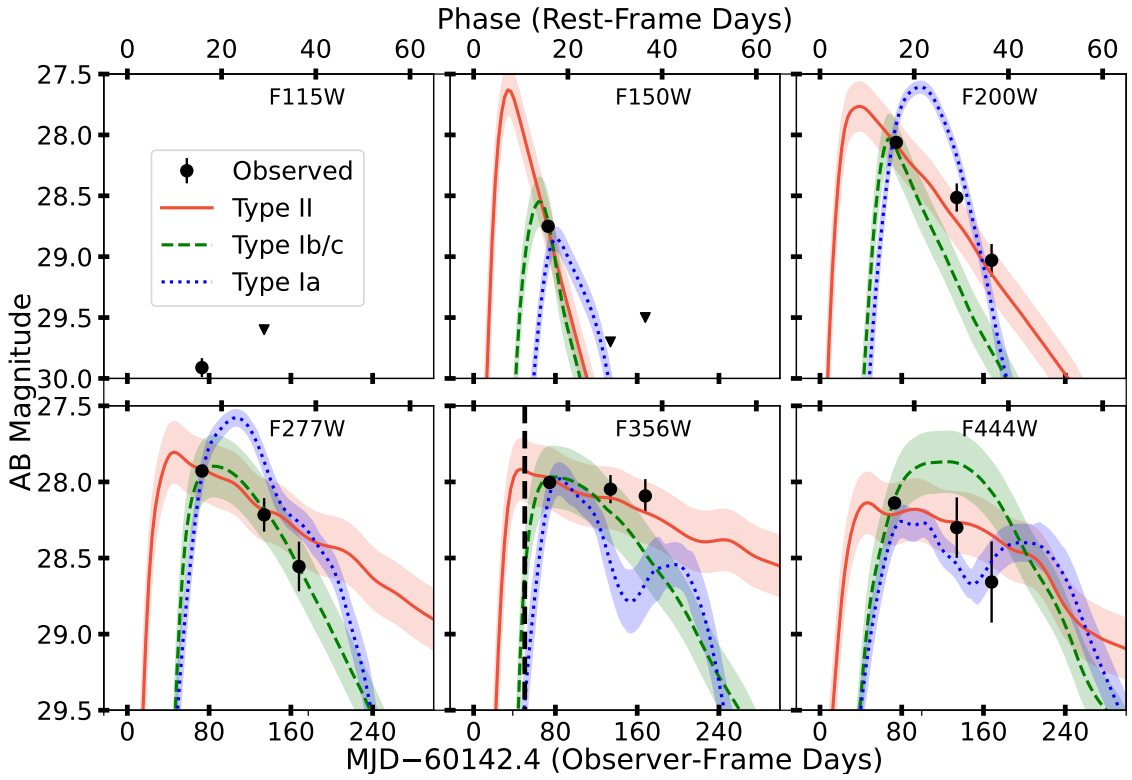

Figure 3. The photometry measured in Section 2.1 is shown as black circles with errors, with (2σ) upper-limits denoted by triangles. The best fit SN II (red solid line), SN Ib/c (green dashed line), and SN Ia (blue dotted line) models are shown for comparison. The SN II model shown is the SN 2006kv template discussed in Section 3.1. The uncertainties shown are purely statistical.

Table 4. `Prospector` Derived Host Properties

Parameter	Value
log(Age [t_*/yr])	$8.55^{+0.15}_{-0.17}$
log(Stellar mass formed [$M_*/M_\odot$])	$8.41^{+0.12}_{-0.12}$
log(SFR/[$M_\odot yr^{-1}$])	$0.31^{+0.08}_{-0.06}$
Gas-Phase Metallicity [$Z_\odot$] *	0.3 ± 0.1
log(O/H) + 12 †	8.1 ± 0.2
A_v [mag]	$0.15^{+0.11}_{-0.07}$

*We derive a gas-phase metallicity using the oxygen line ratio diagnostic O_3O_2 from Curti et al. (2020); see Section 3.2 for a detailed discussion.

†We convert between gas-phase metallicity expressed in solar units to units of log(O/H) + 12 following the relation in Asplund et al. (2009).

However, because there are no clear SN features in the spectrum for AT 2023adsv, yet we know that SN light must be contaminating the spectrum, any fit of the star formation history (SFH) of JADES-GS+53.16439-27.83877 will be biased by this unaccounted for SN light – with the added light leading to systematically higher masses, and the SN color altering the inferred stellar properties. To address this, we perform a fit to the pre-SN photometry for the host galaxy to explore the SFH. We fit the JADES photometry for the source measured from the Hubble Space Telescope (HST) Advanced Camera for Surveys (ACS) in filters F435W, F606W, F775W, F814W, and F850LP along with JWST/NIRCam in the filters F090W, F115W, F150W, F182M, F200W, F210M, F277W, F335M, F356W, F410M, and F444W. For the fit,

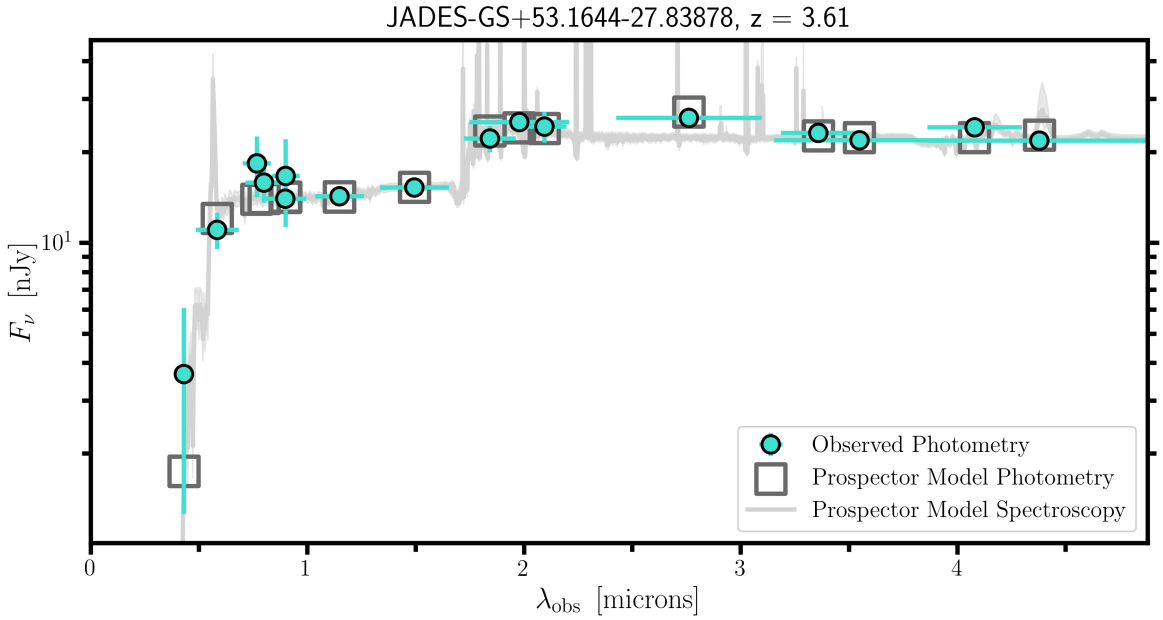

Figure 4. Host template photometry fit using `Prospector`. The blue circles represent the observed JADES pre-SN photometry, and the dark grey shaded line represents the 50th percentile of the final `Prospector` fit to the photometry, with a lighter grey color showing the 16th and 84th percentiles on the fit. The grey boxes are the estimated `Prospector` photometry corresponding to the fit. We provide the derived `Prospector` host galaxy parameters in Table 4.

we use the tool `Prospector`[7] (Johnson et al. 2021) and follow the method outlined in Helton et al. (in preparation). Briefly, within `Prospector` we employ the Flexible Stellar Population Synthesis (FSPS) code (Conroy et al. 2009; Conroy & Gunn 2010), and we sampled the posterior distributions of the stellar population properties using the dynamic nested sampling code `dynesty`[8] (Speagle 2020). We utilize a Chabrier initial mass function (IMF) with a lower bound of 0.08 $M_\odot$ and an upper bound of 120 $M_\odot$. Additionally, we assume a delayed-τ star-forming history of the form $\mathrm{SFR} \sim t_{\rm age} \times e^{-t_{\rm age}/\tau}$, where SFR is the star formation rate, $t_{\rm age}$ is the age of the galaxy, and τ is the e-folding time. For the fit, we fix the redshift to $z = 3.61$, and allow the stellar- and gas-phase metallicity to vary uniformly between $\log(Z/Z_\odot) = -3.0 - 0.0$. We plot the `Prospector` fit corresponding to the 50th percentile on the posterior, along with the fit photometry, in Figure 4.

From these fits we estimate a host mass of $\log_{10}(M_*/M_\odot) = 8.41^{+0.12}_{-0.12}$, host age $\log_{10}(t_*/yr) = 8.55^{+0.15}_{-0.17}$, and host extinction $A_v = 0.15^{+0.11}_{-0.07}$ mag. These and additional host properties are summarized in Table 4.

Because there are no clear SN features in the spectrum for AT 2023adsv, we rely on the metallicity inferred from the host to estimate the metallicity of the SN. However, while we use `Prospector` to infer host properties like mass, we do not use it to infer the host metallicity because the host SED modeling can be unreliable due to the strong degeneracy between metallicity and stellar age (Dotter et al. 2017). To infer the host metallicity, we instead turn to spectral fitting of the forbidden oxygen lines present in the spectrum (see Figure 2). In the photospheric phase, we do not expect much SN contamination in [O II] and [O III], and use

[7] https://prospect.readthedocs.io/en/stable/
[8] https://dynesty.readthedocs.io/en/stable/

the ratio of [O III] to [O II] (i.e., the O_3O_2 diagnostic from Curti et al. (2020)) to estimate the metallicity at the position of the SN. We find that $O_3O_2 = 3.0^{+3.2}_{-1.1}$, and assuming a solar metallicity of $\log(O/H) + 12 = 8.69$ (Asplund et al. 2009), we find a host oxygen abundance of $\log(O/H) + 12 = 8.1 \pm 0.2$, or $Z_* \approx 0.3\ Z_\odot$. We note that `Prospector` finds a gas-phase metallicity of $\log(O/H)+12 = 7.1\pm0.1$, or $Z_* \approx 0.02\ Z_\odot$, $\sim$ an order of magnitude lower. This is a substantial discrepancy, however, we adopt the derivation from the oxygen ratio due to the aforementioned issues when using the integrated fit from `Prospector`. For the remainder of the paper, we adopt a gas-phase metallicity of $\log(O/H) + 12 = 8.1 \pm 0.2$. This metallicity is notably lower than the mean derived oxygen metallicity found for a collection of SNe II (dominated by IIP) by Anderson et al. (2010) of $\log(O/H) + 12 = 8.580 \pm 0.027$.

We place this galaxy in a wider context of SNe II hosts in Figure 5. We compare the mass and metallicity of the host of AT 2023adsv with a population of $z < 0.7$ galaxies from SDSS DR8 (grey contours; Aihara et al. 2011; Eisenstein et al. 2011), galaxies from *JWST* with redshifts $3 \leq z \leq 9$ (yellow-pink points; Nakajima et al. 2023; Morishita et al. 2024; Curti et al. 2024), core-collapse SN hosts (purple points; Kelly & Kirshner 2012), and low-metallicity dwarf galaxies (blue points; Berg et al. 2012). Metallicities for both the SN hosts and SDSS sample were derived following the PP04 O3N2 calibration from Pettini & Pagel (2004), while metallicities for both the *JWST*-selected, high-z sample and dwarf sample were derived using the direct electron-temperature method (Campbell et al. 1986). Over-plotted are horizontal dashed lines corresponding to the the 1.0, 0.3, and 0.1 solar oxygen abundance values converted from Asplund et al. (2009), as well as the mass-metallicity relationship (MZR) for galaxies at $2.65 \geq z \geq 3.4$ from Li et al. (2023, red dashed line), and the MZR at $3 \geq z \geq 10$ from Curti et al. (2024, green dashed line). These MZR scalings are supported by recent work with *JWST* (Schaerer et al. 2022; Taylor et al. 2022; Katz et al. 2023; Rhoads et al. 2023), tracing this relation to even further distances with measurements of two galaxies at $z \approx 8$, and has confirmed that at fixed stellar mass, galaxies are generally less enriched at higher redshift (Langeroodi et al. 2023). We find that the metallicity of the host of AT 2023adsv is consistent with the MZR from Li et al. (2023) as well as with the lower-metallicity tail of the core-collapse distribution.

3.3. *Light curve Modeling*

In order to estimate the explosion properties of AT 2023adsv, we compare synthetic light curves with those of AT 2023adsv. For this purpose, we first obtained red supergiant (RSG) SN progenitor models with 0.3 $Z_\odot$ (in agreement with the inferred metallicity measured for its host; see Section 3.2) by using `Modules for Experiments in Stellar Astrophysics (MESA)` version r23.05.1 (Paxton et al. 2011, 2013, 2015, 2018, 2019; Jermyn et al. 2023). We selected a grid of models with zero-age main-sequence (ZAMS) masses (M_{ZAMS}) of 12, 16, and 20 $M_\odot$. The details of the assumptions in the stellar evolution calculations are presented by the accompanying paper (Moriya et al., in preparation). The final progenitor properties are summarized in Table 5.

The RSG progenitor models are then transferred to the one-dimensional multi-frequency radiation hydrodynamics code `STELLA` (Blinnikov et al. 1998, 2000, 2006). `STELLA` numerically evaluates the SED evolution of SNe, and thus we can directly estimate light curves in the observer frame from the theoretical SED evolution when they appear at $z = 3.6$. We refer to the accompanying paper for the details on the light curve calculations (Moriya et al., in preparation). Because SNe II are generally found to be embedded within a dense and confined circumstellar medium (CSM; e.g., Förster et al. 2018), we also include a version of each of our models with this close in CSM (deposited up to 10^{15} cm). This approach was

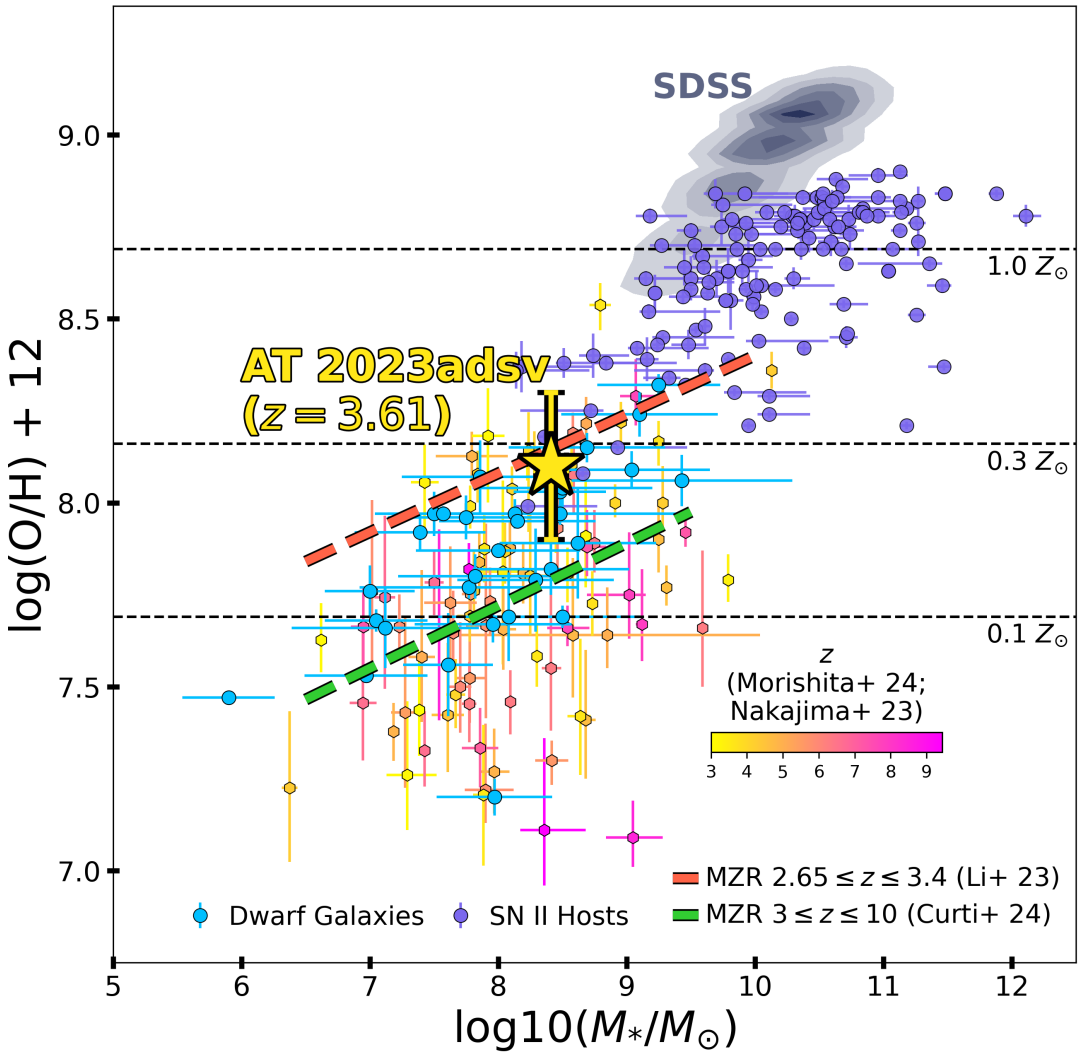

Figure 5. AT 2023adsv's inferred host galaxy mass and metallicity (gold star) compared to a selection of local galaxies. Grey contours correspond to galaxies selected from SDSS DR8 with $z < 0.7$ (Aihara et al. 2011; Eisenstein et al. 2011), purple points correspond to core-collapse SN hosts (Kelly & Kirshner 2012), yellow-pink points correspond to *JWST*-selected galaxies redshifts at $3 \leq z \leq 9$ (Nakajima et al. 2023; Curti et al. 2024; Morishita et al. 2024), and blue points correspond to low-metallicity dwarf galaxies from Berg et al. (2012). The red dashed line corresponds to the mass-metallicity relationship (MZR) for galaxies at $2.65 \leq z \leq 3.4$ from Li et al. (2023); the green dashed line corresponds to the MZR at $3 \leq z \leq 10$ from Curti et al. (2024). Overplotted are horizontal dashed lines which correspond to the the 1.0, 0.3, and 0.1 solar oxygen abundance values derived from Asplund et al. (2009).

taken to account for the amount of UV flux detected in the first epoch (i.e., at $z = 3.6$, F115W and F150W span $\sim 2500 - 3250$ Å in the rest-frame), and the fact that a typical mass-loss rate of 10^{-3} $M_\odot$ yr^{-1} with a wind velocity of 10 km s^{-1}, can act as an additional early power source in the light curve (Moriya et al. 2011; Dessart & Hillier 2022). The confined CSM mass is 0.07 $M_\odot$ ($M_{\rm ZAMS} = 12M_\odot$), 0.11 $M_\odot$ ($M_{\rm ZAMS} = 16M_\odot$), and 0.16 $M_\odot$ ($M_{\rm ZAMS} = 20M_\odot$).

Figure 6 presents the results of the numerical modeling. We find that an explosion energy of $(2 - 3) \times 10^{51}$ erg is required to account for the brightness of AT 2023adsv. While the three progenitor models explain the overall properties of AT 2023adsv well, the $12M_\odot$ and $16M_\odot$ models

without CSM struggle to reproduce the observed UV flux in the first epoch. In the models with CSM, both the $12\mathrm{M}_\odot$ and $16\mathrm{M}_\odot$ models do better at matching the early-time UV flux, but are underluminous compared to the first detections in F277W, F356W, and F444W despite boosting their explosion energies to 2.5×10^{51} ergs. All models fail to fit the last epoch F200W, F277W, and F444W detections. Despite this, we find that the best overall fit to be the $20\mathrm{M}_\odot$ progenitors (both with and without CSM), and cannot distinguish between them due to not having observations during the timeframe of the inferred modeled peak.

3.3.1. *Pair-Instability Explosion*

Motivated by exploring an alternative explanation for the measured early blue flux at the redshift of AT 2023adsv, as well as the prediction that PISNe could form at metallicities as high as $\mathrm{Z}_\odot/3$ (the metallicity of AT 2023adsv's host; Langer et al. 2007), we compared PISN light-curve models from Kasen et al. (2011) to our measured photometry. We found that the 175 $\mathrm{M}_\odot$ RSG PISN model (R175) matches well to AT 2023adsv, but that the dataset as it stands is not sufficient to differentiate between a PISN model and those explored in (Fig. 7). The PISN has a much longer duration than typical RSG explosions discussed before, so more observations at later times would be required to confirm (or rule out) a PISN progenitor. Because of the expected low PISN event rates, AT 2023adsv is likely to be a RSG explosion. However, future wide-area surveys will be able to discover PISNe and high-z SNe II such as AT 2023adsv, demonstrating the importance of long-term monitoring of the same field in order to distinguish between PISNe and other typical SNe.

3.4. *Color-Magnitude Comparison*

In Figure 8 we plot the observed colors vs observed F356W (rest-frame $\sim$ I-band) magnitude of the best RSG models ($20\ \mathrm{M}_\odot$ with and without CSM interaction), along with SN 2006kv, a normal SN IIP and the best fit spectral template match found in Section 3.1. The shape of each marker corresponds to the epoch of the observation, with the circle, square, and star corresponding to the first, second, and third observed epochs listed in Table 1. Triangles are upper-limit measurements. The colored lines track the corresponding color-magnitude evolution of each model as a function of time, where the color of the line reflects the observer-frame days relative to the B-band peak for these models. From this evolution plot, SN 2006kv shows a striking similarity. We leverage this similarity when comparing AT 2023adsv to a collection of local SNe IIP in Section 4.1.

Table 5. Progenitor properties for light-curve computations.

M_{ZAMS} ($\mathrm{M}_\odot$)	M_{fin} ($\mathrm{M}_\odot$)	$M_{\mathrm{H-rich}}$ ($\mathrm{M}_\odot$)	R_{fin} ($\mathrm{R}_\odot$)
12	11.8	8.6	434
16	14.7	10.0	632
20	15.9	9.5	847
175	163.8	79.4	2499

NOTE—Columns are: ZAMS mass (M_{ZAMS}), final mass at explosion (M_{fin}), hydrogen-rich envelope mass at explosion ($M_{\mathrm{H-rich}}$), and progenitor radius at explosion (R_{fin}).

4. DISCUSSION

4.1. *AT 2023adsv's Metallicity and Comparison to Low-z SN IIPs*

The question of metallicity is a central one when considering the likely explosion scenario for AT 2023adsv, as well as in understanding the physical origin of its bright UV luminosity in the first *JWST* epoch. In particular, higher metallicities can lead to more pre-SN mass loss via line-driven stellar winds (Mokiem et al. 2007), a lower mass hydrogen envelope (and therefore a shorter duration plateau phase of a SN IIP), and a smaller ejecta mass of the explosion. Depending on the location, density, and distribution of this wind-driven material, the SN shock breakout from core-collapse

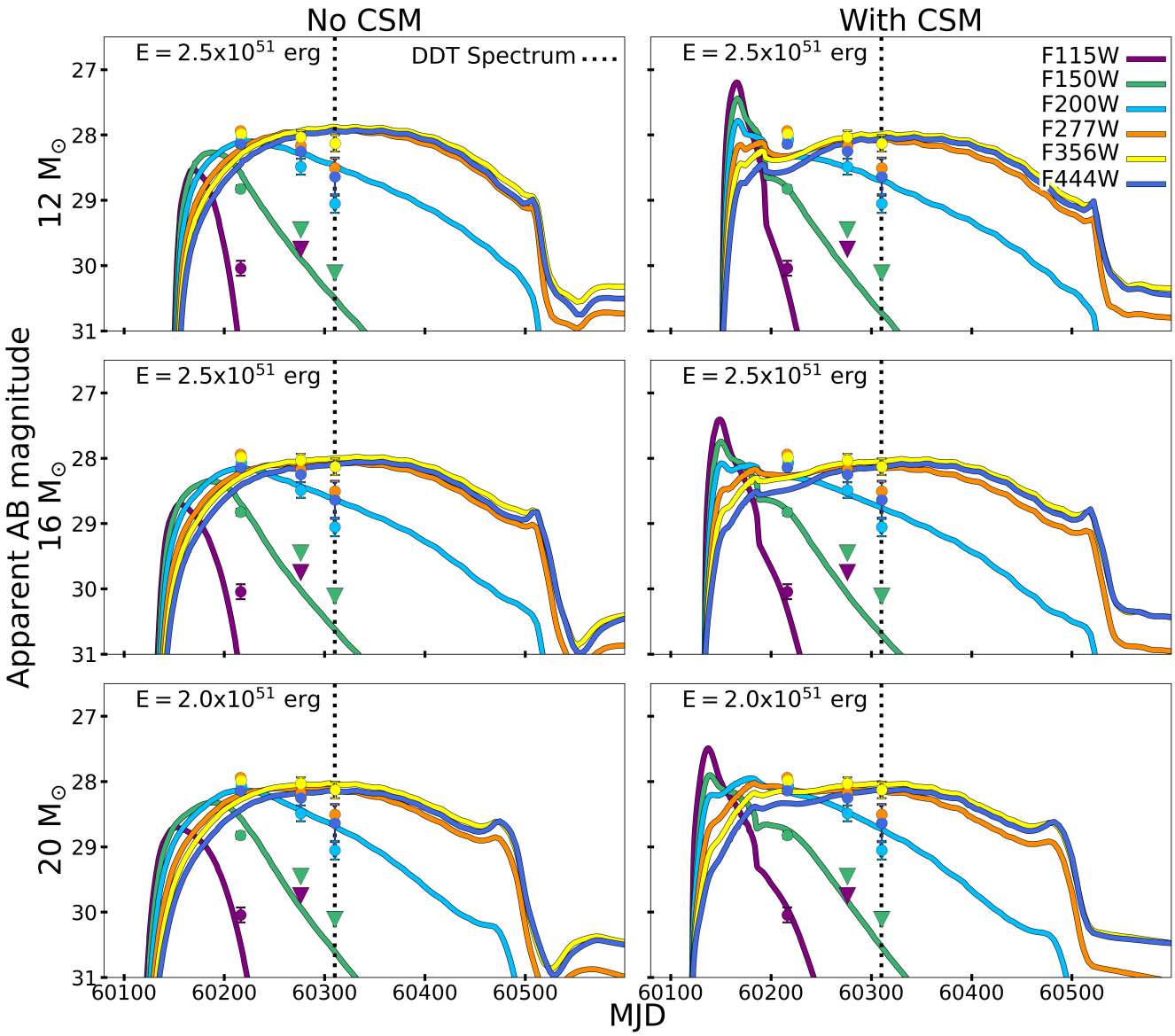

Figure 6. A grid of light-curve models for AT 2023adsv based on the 0.3 $Z_\odot$ RSG SN progenitors used in this study. Each row corresponds to a different ZAMS mass (from the top to bottom row: 12, 16, and 20 $M_\odot$) with the left column free from confined CSM, and the right column containing a confined CSM mass of 0.07 $M_\odot$ (12 $M_\odot$), 0.11 $M_\odot$ (16 $M_\odot$), and 0.16 $M_\odot$ (20 $M_\odot$) at a radius of 10^{15} cm. We vary the explosion energy between $2.0 - 3.0 \times 10^{51}$ erg. The higher mass models better match the range of observations of AT 2023adsv than the models with $M < 20 M_\odot$, although we cannot distinguish between the models with and without CSM. A more complete discussion is presented in Section 3.3. The vertical dashed line represents the time of the DDT spectrum.

can be extended from a baseline of 1-1000 seconds to many hours (Gezari et al. 2015; Förster et al. 2018), and at high-z these same effects could span *days* in the observer-frame. In general, this interaction between the shock and the surrounding CSM can lead to an increased UV and optical luminosity in the observed light curve (Schlegel 1990; Moriya et al. 2011). Lower metallicity, on the other hand, will lower the opacity of the envelope, resulting in hotter and more compact stars. This lower opacity decreases the line blanketing of the UV portion of the spectrum, allowing more blue light to escape the SN (Eastman et al. 1994; Dessart et al. 2013).

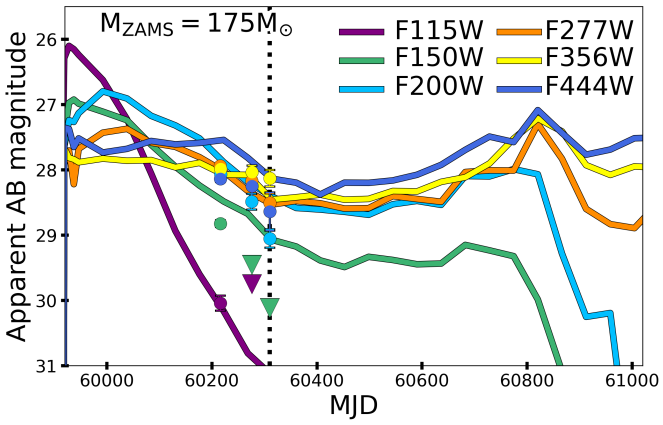

Figure 7. AT 2023adsv compared with the RSG PISN model (R175) from Kasen et al. (2011). While the PISN model fit is reasonable for AT 2023adsv, long term monitoring of this object would be needed to distinguish whether AT 2023adsv is a typical SNe or a more exotic PISN.

However, indirectly ascertaining an SN IIP's metallicity from its light curve, e.g. by studying its luminosity and color evolution, is further complicated by the degeneracy of this evolution with the effect that the progenitor's radius has on its explosion properties. Specifically, during the SN explosion, the expansion from a smaller radius contributes to faster cooling and therefore faster color evolution during the photospheric phase; this radius is in turn sensitive to effects like stellar rotation, convective overshoot, and mixing (see Dessart et al. (2013) for a review). For these reasons, and owing to the fact that the outermost ejecta of SNe IIP have photospheres which are characterized by the molecular clouds from which the pre-SN stars are formed (Dessart et al. 2014), definitive assessments of an SN IIP's metallicity are done through detailed spectroscopic studies of the strengths of metal-line absorptions during an SN IIP's plateau phase (Dessart & Hillier 2020). In particular, the 'pseudo' equivalent width (pEW) of Fe II λ5018 Å has been shown as a proxy for the metallicity of an SN IIP, with larger widths suggesting higher metallicities. This result has been confirmed observationally in the local universe (Anderson et al. 2016; Taddia et al. 2016; Gutiérrez et al. 2017, 2018), but relies on spectral coverage during the plateau phase to accurately measure the effect.

In our analysis of AT 2023adsv, we do not have a spectrum with distinct SN features to perform this measurement, but an intriguing study by Scott et al. (2019, hereafter, S19) finds that when comparing the plateau luminosity of a sample of SN IIP with their host luminosity (in rest-frame r-band), spectroscopically-confirmed, low metallicity SNe IIP tend to separate from a "control" sample taken from the literature. Specifically, S19's sample are constructed from "high-contrast" SN IIP — those with high SN luminosities but with low luminosity hosts, versus a sample of SN IIP without this property. The central idea is to test the assertion that these high-contrast SN IIP also have low metallicities as measured in spectra taken during their plateau phase (i.e., because of the inferred low metallicity of low luminosity hosts via the MZR). S19's result confirms this statistically, and crucially, S19 compares the low-metallicity sample with the control sample photometrically.

Motivated by this, and because AT 2023adsv is well-modeled by SN 2006kv, we fit the last observed epoch of AT 2023adsv (F200W, F277W, F356W, and F444W) with a blackbody and find a temperature of $\sim$ 6200 K — within the range of the recombination temperatures of H which power the plateau-phase of an SN IIP's light curve (5500 $-$ 7000 K; Dessart et al. 2014; Dessart & Hillier 2020). Therefore, if we assume that AT 2023adsv *is* an SN IIP and is within or *near* the plateau-phase in the last observed *JWST* epoch, we can provisionally compare AT 2023adsv with the sample in S19. We perform k-corrections on both the host and SN photometry, and find that the fitted SN 2006kv model's luminosity at $+50$ days is -17.5 Mag in r-band. The resulting comparison is shown in Figure 9.

In this parameter space, AT 2023adsv's high luminosity places its abscissa in the same region as the low-metallicity SNe IIP selected by S19, how-

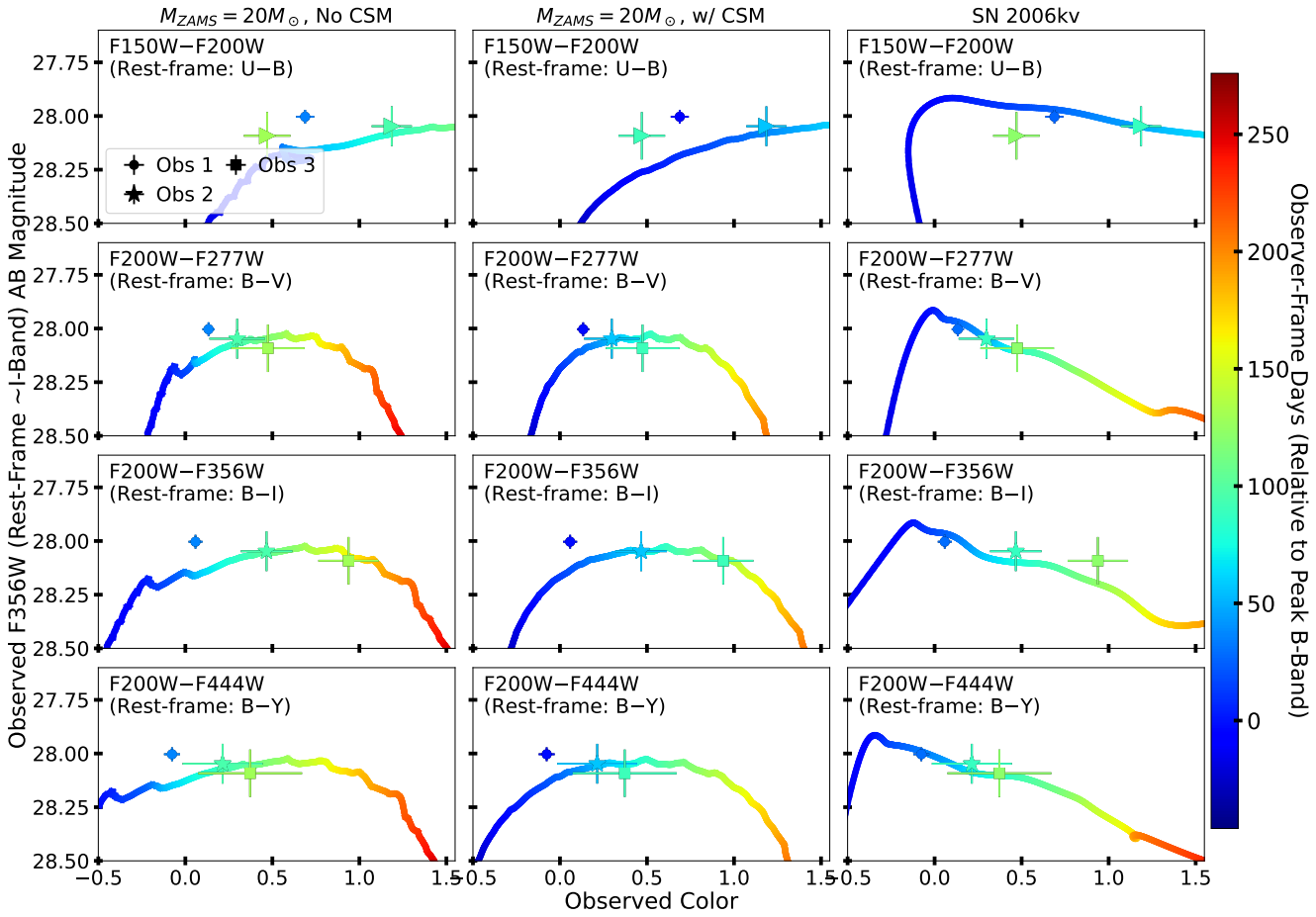

Figure 8. Four observed colors (labeled by row) vs. magnitude (F356W, rest-frame ∼I-band) shown in the legend as black points with error bars, with the symbols corresponding to the three observed epochs (a legend in upper-left; order of observations is circle, star, square), and limits shown with directional arrows. The colored lines (and the fill color of the symbols) track the corresponding color-magnitude space as a function of time from best fit models, with MESA models from Section 3.3 in the first two columns and the best spectral template fit (SN 2006kv) in the third column (see Section 3.1). The coloring of the lines is described by the color bar (right), with early times shown as blue and late times as red.

ever, AT 2023adsv's host brightness places its ordinate between the control sample and the low-metallicity sample. The apparent tension of an "overluminous" host for a lower-metallicity SN IIP can be related to the the result presented in Figure 5. In the context of an MZR that evolves with redshift (see Section 3.2), we expect that at a fixed stellar-mass, O/H decreases with increasing redshift, which for a host at $3 \leq z \leq 4$ would move AT 2023adsv's host luminosity closer to the control (i.e., higher metallicity) sample.

5. CONCLUSION

We have presented *JWST* observations of AT 2023adsv with a spectroscopic redshift of $z = 3.613 \pm 0.001$, which we classify using light curve information as a relatively bright ($M_B = -18.3 \pm 0.1$mag) SN II. We further model the light

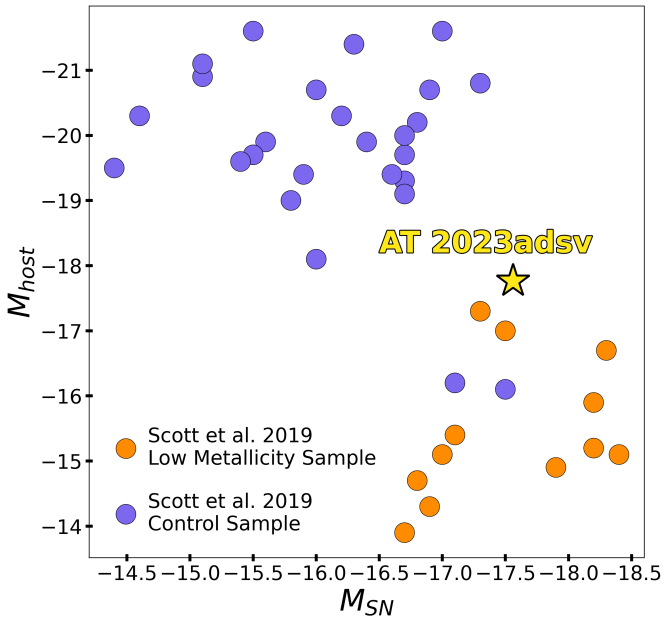

Figure 9. Figure adapted from Scott et al. (2019), with a sample of local, low-metallicity selected SN IIP (orange points) compared to a "control" sample of local, SN IIP from the literature (purple points). All photometry is reported in r-band, and SN luminosities are taken during the plateau phase. The gold star corresponds to an estimate of AT 2023adsv's plateau luminosity were it an SN IIP (see Section 4.1) along with its host luminosity, which occupies a space between the two samples.

curve using the MESA code and find a good match to a RSG progenitor star with ZAMS mass $20M_{\odot}$, albeit with a slightly high explosion energy of 2.0×10^{51} ergs. AT 2023adsv could also plausibly be a PISN, but such a rare object is a less likely explanation than a normal SN II, and more observations with a longer temporal baseline would be necessary to confirm or rule out such a result.

While the DDT spectrum of AT 2023adsv confirms its redshift, we could not reliably isolate specific SN features in the spectrum, and we limited our our analysis of AT 2023adsv and JADES-GS+53.16439-27.83877 to their photometric properties to prevent bias. Examining the host of AT 2023adsv, JADES-GS+53.16439-27.83877, we find a relatively low-mass ($\log_{10}(M_*/M_{\odot}) = 8.41^{+0.12}_{-0.12}$), moderately dusty ($A_v = 0.15^{+0.11}_{-0.07}$ mag), low-metallicity ($Z_* = 0.3 \pm 0.1\ Z_{\odot}$) galaxy. A more careful study of the host environment, and potentially of the SN itself, would be possible with a template spectrum of the host with the same observing parameters in a future *JWST* cycle – allowing a direct comparison of a spectrum with, and without, contaminating SN light.

AT 2023adsv is likely the most distant SN II with a spectroscopic redshift yet found (although see AT 2023adst, a reported SN II with a host $z = 4.117$, yet with a much less robust classification; DeCoursey et al. 2024), and provides a timely opportunity to study massive SN progenitors at $z > 3$. Intriguingly, AT 2023adsv's inferred metallicity places it in a parameter space between that of low-z, low-metallicity SNe IIP and a control sample of solar metallicity SNe IIP hosted in massive galaxies; it will be necessary to continue to observe such distant CC SNe with *JWST* to statistically test whether such CC SNe are indeed well-modeled by massive and metal poor progenitors with higher than average explosion energies. Carefully following up these high-z SNe may lead to novel constraints on the early Universe IMF, as well as metal enrichment and mixing. Upcoming surveys such as the *Nancy Grace Roman Space Telescope* High Latitude Time Domain Survey (HLTDS; Hounsell et al. 2018; Rose et al. 2021) will likely open a new frontier for this science by finding thousands of distant massive progenitor CC SNe. However, *JWST* will remain our only resource capable of rest-frame optical-IR imaging and spectroscopy at high-z, highlighting the need for building a sample of such observations now and into the future.

Acknowledgments

This paper is based in part on observations with the NASA/ESA/CSA *Hubble Space Telescope* and *James Webb Space Telescope* obtained from the Mikulski Archive for Space Telescopes at Space Telescope Science Institute (STScI), which is operated by the Association of Universities for Research in Astronomy, Inc. (AURA), under

NASA contract NAS 5-03127 for *JWST*. These observations are associated with program #1180 and #6541. We thank the DDT and *JWST*/*HST* scheduling teams at STScI for their extraordinary effort in getting the DDT observations used here scheduled quickly. The specific observations analyzed can be accessed via DOI: 10.17909/snj9-an10; support was provided to JDRP and ME through program HST-GO-16264. JDRP is supported by NASA through a Einstein Fellowship grant No. HF2-51541.001 awarded by STScI, which is operated by AURA, for NASA, under contract NAS5-26555. Numerical computations were in part carried out on PC cluster at the Center for Computational Astrophysics, National Astronomical Observatory of Japan. TJM is supported by the Grants-in-Aid for Scientific Research of the Japan Society for the Promotion of Science (JP24K00682, JP24H01824, JP21H04997, JP24H00002, JP24H00027, JP24K00668) and by the Australian Research Council (ARC) through the ARC's Discovery Projects funding scheme (project DP240101786). AJB acknowledges funding from the "FirstGalaxies" Advanced Grant from the European Research Council (ERC) under the European Union's Horizon 2020 research and innovation program (Grant agreement No. 789056). DJE is supported as a Simons Investigator and by *JWST*/NIRCam contract to the University of Arizona, NAS5-02015. BDJ acknowledges the *JWST*/NIRCam contract to the University of Arizona, NAS5-02015. RM acknowledges support by the Science and Technology Facilities Council (STFC), by the ERC through Advanced Grant 695671 "QUENCH", and by the UKRI Frontier Research grant RISEandFALL. RM also acknowledges funding from a research professorship from the Royal Society. BER acknowledges support from the NIRCam Science Team contract to the University of Arizona, NAS5-02015, and *JWST* Program 3215. ST acknowledges support by the Royal Society Research Grant G125142. QW is supported by the Sagol Weizmann-MIT Bridge Program. The authors acknowledge use of the lux supercomputer at UC Santa Cruz, funded by NSF MRI grant AST 1828315.

REFERENCES

Aihara, H., Allende Prieto, C., An, D., et al. 2011, ApJS, 193, 29, doi: 10.1088/0067-0049/193/2/29

Anderson, J. P., Covarrubias, R. A., James, P. A., Hamuy, M., & Habergham, S. M. 2010, MNRAS, 407, 2660, doi: 10.1111/j.1365-2966.2010.17118.x

Anderson, J. P., Gutiérrez, C. P., Dessart, L., et al. 2016, A&A, 589, A110, doi: 10.1051/0004-6361/201527691

Asplund, M., Grevesse, N., Sauval, A. J., & Scott, P. 2009, ARA&A, 47, 481, doi: 10.1146/annurev.astro.46.060407.145222

Bazin, G., Palanque-Delabrouille, N., Rich, J., et al. 2009, A&A, 499, 653, doi: 10.1051/0004-6361/200911847

Becker, A. 2015, HOTPANTS: High Order Transform of PSF ANd Template Subtraction

Berg, D. A., Skillman, E. D., Marble, A. R., et al. 2012, ApJ, 754, 98, doi: 10.1088/0004-637X/754/2/98

Blinnikov, S., Lundqvist, P., Bartunov, O., Nomoto, K., & Iwamoto, K. 2000, ApJ, 532, 1132, doi: 10.1086/308588

Blinnikov, S. I., Eastman, R., Bartunov, O. S., Popolitov, V. A., & Woosley, S. E. 1998, ApJ, 496, 454, doi: 10.1086/305375

Blinnikov, S. I., Röpke, F. K., Sorokina, E. I., et al. 2006, A&A, 453, 229, doi: 10.1051/0004-6361:20054594

Botticella, M. T., Riello, M., Cappellaro, E., et al. 2008, A&A, 479, 49, doi: 10.1051/0004-6361:20078011

Burrows, A., & Vartanyan, D. 2021, Nature, 589, 29, doi: 10.1038/s41586-020-03059-w

Bushouse, H., Eisenhamer, J., Dencheva, N., et al. 2022, JWST Calibration Pipeline, Zenodo, doi: 10.5281/zenodo.7325378

Campbell, A., Terlevich, R., & Melnick, J. 1986, MNRAS, 223, 811, doi: 10.1093/mnras/223.4.811

Chen, W., Kelly, P. L., Oguri, M., et al. 2022, Nature, 611, 256, doi: 10.1038/s41586-022-05252-5

Conroy, C., & Gunn, J. E. 2010, ApJ, 712, 833, doi: 10.1088/0004-637X/712/2/833

Conroy, C., Gunn, J. E., & White, M. 2009, ApJ, 699, 486, doi: 10.1088/0004-637X/699/1/486

Cooke, J., Sullivan, M., Gal-Yam, A., et al. 2012, Nature, 491, 228, doi: 10.1038/nature11521

Curti, M., Mannucci, F., Cresci, G., & Maiolino, R. 2020, MNRAS, 491, 944, doi: 10.1093/mnras/stz2910

Curti, M., Maiolino, R., Curtis-Lake, E., et al. 2024, A&A, 684, A75, doi: 10.1051/0004-6361/202346698

Dahlen, T., Strolger, L.-G., Riess, A. G., et al. 2012, ApJ, 757, 70, doi: 10.1088/0004-637X/757/1/70

DeCoursey, C., Egami, E., Rieke, M., et al. 2023a, Transient Name Server AstroNote, 164, 1

DeCoursey, C., Sun, F., Egami, E., et al. 2023b, Transient Name Server AstroNote, 275, 1

DeCoursey, C., Egami, E., Rieke, M., et al. 2023c, Transient Name Server AstroNote, 164, 1

DeCoursey, C., Egami, E., Pierel, J. D. R., et al. 2024, arXiv e-prints, arXiv:2406.05060

Dessart, L., & Hillier, D. J. 2020, A&A, 642, A33, doi: 10.1051/0004-6361/202038148

—. 2022, A&A, 660, L9, doi: 10.1051/0004-6361/202243372

Dessart, L., Hillier, D. J., Waldman, R., & Livne, E. 2013, MNRAS, 433, 1745, doi: 10.1093/mnras/stt861

Dessart, L., Gutierrez, C. P., Hamuy, M., et al. 2014, MNRAS, 440, 1856, doi: 10.1093/mnras/stu417

Dotter, A., Conroy, C., Cargile, P., & Asplund, M. 2017, ApJ, 840, 99, doi: 10.3847/1538-4357/aa6d10

D'Andrea, C. B., Sako, M., Dilday, B., et al. 2010, The Astrophysical Journal, 708, 661, doi: 10.1088/0004-637X/708/1/661

Eastman, R. G., Woosley, S. E., Weaver, T. A., & Pinto, P. A. 1994, ApJ, 430, 300, doi: 10.1086/174404

Egami, E., Bonaventura, N., Charlot, S., et al. 2023, JWST NIRSpec/NIRCam Follow-Up of the High-Redshift Transients Discovered in the GOODS-S JADES-Deep Field

Eisenstein, D. J., Weinberg, D. H., Agol, E., et al. 2011, AJ, 142, 72, doi: 10.1088/0004-6256/142/3/72

Eisenstein, D. J., Johnson, B. D., Robertson, B., et al. 2023, arXiv e-prints, arXiv:2310.12340, doi: 10.48550/arXiv.2310.12340

Eisenstein, D. J., Willott, C., Alberts, S., et al. 2023, arXiv e-prints, arXiv:2306.02465, doi: 10.48550/arXiv.2306.02465

Engesser, M., Smith, K., Chen, T., et al. 2022a, Transient Name Server AstroNote, 155, 1

Engesser, M., Brammer, G., Gould, K., et al. 2022b, Transient Name Server AstroNote, 145, 1

Ferruit, P., Jakobsen, P., Giardino, G., et al. 2022, A&A, 661, A81, doi: 10.1051/0004-6361/202142673
Fitzpatrick, E. 1999, Publications of the Astronomical Society of the Pacific, 111, 63, doi: 10.1086/316293
Förster, F., Moriya, T. J., Maureira, J. C., et al. 2018, Nature Astronomy, 2, 808, doi: 10.1038/s41550-018-0563-4
Fruchter, A. S., Levan, A. J., Strolger, L., et al. 2006, Nature, 441, 463, doi: 10.1038/nature04787
Gal-Yam, A. 2019, ARA&A, 57, 305, doi: 10.1146/annurev-astro-081817-051819
Gal-Yam, A., Arcavi, I., Ofek, E. O., et al. 2014, Nature, 509, 471, doi: 10.1038/nature13304
Gezari, S., Jones, D. O., Sanders, N. E., et al. 2015, ApJ, 804, 28, doi: 10.1088/0004-637X/804/1/28
Giavalisco, M., Ferguson, H. C., Koekemoer, A. M., et al. 2004, ApJL, 600, L93, doi: 10.1086/379232
Gomez, S., Nicholl, M., Berger, E., et al. 2024, MNRAS, 535, 471, doi: 10.1093/mnras/stae2270
Graur, O., Poznanski, D., Maoz, D., et al. 2011, MNRAS, 417, 916, doi: 10.1111/j.1365-2966.2011.19287.x
Grogin, N. A., Kocevski, D. D., Faber, S. M., et al. 2011, ApJS, 197, 35, doi: 10.1088/0067-0049/197/2/35
Gutiérrez, C. P., Anderson, J. P., Hamuy, M., et al. 2017, ApJ, 850, 89, doi: 10.3847/1538-4357/aa8f52
Gutiérrez, C. P., Anderson, J. P., Sullivan, M., et al. 2018, MNRAS, 479, 3232, doi: 10.1093/mnras/sty1581
Heger, A., Fryer, C. L., Woosley, S. E., Langer, N., & Hartmann, D. H. 2003, ApJ, 591, 288, doi: 10.1086/375341
Horne, K. 1986, PASP, 98, 609, doi: 10.1086/131801
Hounsell, R., Scolnic, D., Foley, R. J., et al. 2018, The Astrophysical Journal, 867, 23, doi: 10.3847/1538-4357/aac08b
Jermyn, A. S., Bauer, E. B., Schwab, J., et al. 2023, ApJS, 265, 15, doi: 10.3847/1538-4365/acae8d
Johnson, B. D., Leja, J., Conroy, C., & Speagle, J. S. 2021, ApJS, 254, 22, doi: 10.3847/1538-4365/abef67
Kasen, D., Woosley, S. E., & Heger, A. 2011, ApJ, 734, 102, doi: 10.1088/0004-637X/734/2/102
Kasen, D., Woosley, S. E., & Heger, A. 2011, ApJ, 734, 102, doi: 10.1088/0004-637X/734/2/102
Katz, H., Saxena, A., Cameron, A. J., et al. 2023, MNRAS, 518, 592, doi: 10.1093/mnras/stac2657
Kelly, P. L., & Kirshner, R. P. 2012, ApJ, 759, 107, doi: 10.1088/0004-637X/759/2/107
Kobulnicky, H. A., & Skillman, E. D. 1997, ApJ, 489, 636, doi: 10.1086/304830
Koekemoer, A. M., Faber, S. M., Ferguson, H. C., et al. 2011, ApJS, 197, 36, doi: 10.1088/0067-0049/197/2/36
Kudritzki, R.-P., & Puls, J. 2000, ARA&A, 38, 613, doi: 10.1146/annurev.astro.38.1.613
Lamers, H. J. G. L. M., & Cassinelli, J. P. 1999, Introduction to Stellar Winds
Langer, N., Norman, C. A., de Koter, A., et al. 2007, A&A, 475, L19, doi: 10.1051/0004-6361:20078482
Langeroodi, D., Hjorth, J., Chen, W., et al. 2023, ApJ, 957, 39, doi: 10.3847/1538-4357/acdbc1
Larson, R. B. 1998, MNRAS, 301, 569, doi: 10.1046/j.1365-8711.1998.02045.x
Li, M., Cai, Z., Bian, F., et al. 2023, ApJL, 955, L18, doi: 10.3847/2041-8213/acf470
Maeder, A., & Meynet, G. 2012, Reviews of Modern Physics, 84, 25, doi: 10.1103/RevModPhys.84.25
Melinder, J., Dahlen, T., Mencía Trinchant, L., et al. 2012, A&A, 545, A96, doi: 10.1051/0004-6361/201219364
Modjaz, M., Blondin, S., Kirshner, R. P., et al. 2014, AJ, 147, 99, doi: 10.1088/0004-6256/147/5/99
Mokiem, M. R., de Koter, A., Vink, J. S., et al. 2007, A&A, 473, 603, doi: 10.1051/0004-6361:20077545
Morishita, T., Stiavelli, M., Grillo, C., et al. 2024, ApJ, 971, 43, doi: 10.3847/1538-4357/ad5290
Moriya, T., Tominaga, N., Blinnikov, S. I., Baklanov, P. V., & Sorokina, E. I. 2011, MNRAS, 415, 199, doi: 10.1111/j.1365-2966.2011.18689.x
Nakajima, K., Ouchi, M., Isobe, Y., et al. 2023, ApJS, 269, 33, doi: 10.3847/1538-4365/acd556
Oppenheimer, J. R., & Snyder, H. 1939, Physical Review, 56, 455, doi: 10.1103/PhysRev.56.455
Paxton, B., Bildsten, L., Dotter, A., et al. 2011, ApJS, 192, 3, doi: 10.1088/0067-0049/192/1/3
Paxton, B., Cantiello, M., Arras, P., et al. 2013, ApJS, 208, 4, doi: 10.1088/0067-0049/208/1/4
Paxton, B., Marchant, P., Schwab, J., et al. 2015, ApJS, 220, 15, doi: 10.1088/0067-0049/220/1/15
Paxton, B., Schwab, J., Bauer, E. B., et al. 2018, ApJS, 234, 34, doi: 10.3847/1538-4365/aaa5a8
Paxton, B., Smolec, R., Schwab, J., et al. 2019, ApJS, 243, 10, doi: 10.3847/1538-4365/ab2241
Pettini, M., & Pagel, B. E. J. 2004, MNRAS, 348, L59, doi: 10.1111/j.1365-2966.2004.07591.x

Pierel, J. D. R., Rodney, S., Avelino, A., et al. 2018, Publications of the Astronomical Society of the Pacific, 130, 114504, doi: 10.1088/1538-3873/aadb7a
Pierel, J. D. R., Jones, D. O., Kenworthy, W. D., et al. 2022, ApJ, 939, 11, doi: 10.3847/1538-4357/ac93f9
Pierel, J. D. R., Frye, B. L., Pascale, M., et al. 2024a, arXiv e-prints, arXiv:2403.18954, doi: 10.48550/arXiv.2403.18954
Pierel, J. D. R., Newman, A. B., Dhawan, S., et al. 2024b, arXiv e-prints, arXiv:2404.02139, doi: 10.48550/arXiv.2404.02139
Pierel, J. D. R., Engesser, M., Coulter, D. A., et al. 2024c, ApJL, 971, L32, doi: 10.3847/2041-8213/ad6908
Pierel, J. D. R., Coulter, D. A., Siebert, M. R., et al. 2024d, arXiv e-prints, arXiv:2411.11953, doi: 10.48550/arXiv.2411.11953
Postman, M., Coe, D., Benítez, N., et al. 2012, ApJS, 199, 25, doi: 10.1088/0067-0049/199/2/25
Quimby, R. M., Kulkarni, S. R., Kasliwal, M. M., et al. 2011, Nature, 474, 487, doi: 10.1038/nature10095
Rest, A., Pierel, J., Correnti, M., et al. 2023, arminrest/jhat: The JWST HST Alignment Tool (JHAT), Zenodo, doi: 10.5281/zenodo.7892935
Rest, A., Stubbs, C., Becker, A. C., et al. 2005, ApJ, 634, 1103, doi: 10.1086/497060
Rhoads, J. E., Wold, I. G. B., Harish, S., et al. 2023, ApJL, 942, L14, doi: 10.3847/2041-8213/acaaaf
Richardson, D., Jenkins, Robert L., I., Wright, J., & Maddox, L. 2014, AJ, 147, 118, doi: 10.1088/0004-6256/147/5/118
Rose, B. M., Baltay, C., Hounsell, R., et al. 2021, arXiv e-prints, arXiv:2111.03081, doi: 10.48550/arXiv.2111.03081
Sanyal, D., Langer, N., Szécsi, D., -C Yoon, S., & Grassitelli, L. 2017, A&A, 597, A71, doi: 10.1051/0004-6361/201629612
Schaerer, D., Marques-Chaves, R., Barrufet, L., et al. 2022, A&A, 665, L4, doi: 10.1051/0004-6361/202244556
Schlafly, E. F., & Finkbeiner, D. P. 2011, ApJ, 737, 103, doi: 10.1088/0004-637X/737/2/103
Schlegel, E. M. 1990, MNRAS, 244, 269
Scott, S., Nicholl, M., Blanchard, P., Gomez, S., & Berger, E. 2019, ApJL, 870, L16, doi: 10.3847/2041-8213/aaf8ad
Siebert, M. R., Decoursey, C., Coulter, D. A., et al. 2024, arXiv e-prints, arXiv:2406.05076, doi: 10.48550/arXiv.2406.05076
Smartt, S. J. 2009, ARA&A, 47, 63, doi: 10.1146/annurev-astro-082708-101737
Smith, N. 2014, ARA&A, 52, 487, doi: 10.1146/annurev-astro-081913-040025
Speagle, J. S. 2020, MNRAS, 493, 3132, doi: 10.1093/mnras/staa278
Strolger, L.-G., Dahlen, T., Rodney, S. A., et al. 2015, ApJ, 813, 93, doi: 10.1088/0004-637X/813/2/93
Taddia, F., Moquist, P., Sollerman, J., et al. 2016, A&A, 587, L7, doi: 10.1051/0004-6361/201527983
Taylor, A. J., Barger, A. J., & Cowie, L. L. 2022, ApJL, 939, L3, doi: 10.3847/2041-8213/ac959d
Vanbeveren, D., De Loore, C., & Van Rensbergen, W. 1998, A&A Rv, 9, 63, doi: 10.1007/s001590050015
Vink, J. S., de Koter, A., & Lamers, H. J. G. L. M. 2001, A&A, 369, 574, doi: 10.1051/0004-6361:20010127
Woosley, S. E. 2017, ApJ, 836, 244, doi: 10.3847/1538-4357/836/2/244
Woosley, S. E., & Heger, A. 2006, ApJ, 637, 914, doi: 10.1086/498500
Wu, S., & Fuller, J. 2021, ApJ, 906, 3, doi: 10.3847/1538-4357/abc87c
Zeh, A., Klose, S., & Hartmann, D. H. 2004, ApJ, 609, 952, doi: 10.1086/421100
Ziegler, J. J., Edwards, T. D. P., Suliga, A. M., et al. 2022, MNRAS, 517, 2471, doi: 10.1093/mnras/stac2748